An improved model for predicting thermal contact resistance at liquid–solid interface

CrossMark

Chao Yuan, Bin Duan, Lan Li, Bofeng Shang, Xiaobing Luo *

School of Energy and Power Engineering, Huazhong University of Science and Technology, Wuhan 430074, China

ARTICLE INFO

ABSTRACT

Polymeric fluidic thermal interface materials (TIMs) are commonly utilized to reduce the thermal resistance between two solid surfaces in microelectronics. When filling TIMs between the solid surfaces, an amount of air is entrapped between the liquid and solid surfaces, resulting in a thermal contact resistance (R_c) arising at the liquid–solid interface. R_c plays an important role on the thin TIMs with high thermal conductivity, while analytical models for R_c at liquid–solid interface are scarce. Based on former researches, this paper developed an improved predictive model through conducting the wettability analysis at the interface. The model expresses R_c as a function of topography of solid surface, wettability of the liquid on rough surface, mechanics of contact at the interface, and thermal parameters of the contacting bodies. R_c at the TIM-aluminium interface was measured for comparison with the model results. The comparison shows that the model results matches to experimental data within 14.3% when the applied pressure is 0.1 MPa, and the deviations are still within the error bars at higher pressure.

© 2014 Published by Elsevier Ltd.

1. Introduction

Thermal interface materials (TIMs) are commonly used in the thermal management of microelectronics. Polymeric fluidic TIMs, such as thermal greases and phase change materials, are often utilized to reduce the thermal contact resistance (R_c) between the die and the heat spreader, and between the heat spreader and the heat sink [1–3]. Although the polymeric TIMs with high thermal conductivity lead to low bulk thermal resistance (R_{bulk}), thermal resistance at the TIM bond lines is often higher than expected. One of the most important reasons is that when filling the polymeric fluidic materials between the solid surfaces, an amount of air is normally entrapped inside the microcavities of the rough solid surface, resulting in a R_c arising at the liquid–solid interface [1,4]. R_c plays an important role on the thin TIMs with high thermal conductivity [3], while good physical-based analytical models for R_c at liquid–solid surface are still lacking in literatures reviewed carefully in Ref. [3]. It is therefore necessary to develop an effective model to predict it.

Past literatures abound with the models of R_c in solid–solid contact conditions [5–8]. These studies have all concluded that R_c is a function of the surface roughness, asperity slope, mechanical

properties of the solid bodies, apparent area of contact and the compressive load between the contacting surfaces. However, these models are not suitable for the polymeric fluidic TIMs because the mechanical properties, such as Young's modulus or hardness, cannot be defined by the same way [4].

Two approaches have been used to predict R_c according to the limited literatures. One way is to use a numerical model of heat transfer within the solid substrate and the liquid, and to account for temperature gradients within them [9–10]. Bennett and Poulikakos [9] developed a model for estimating thermal contact coefficient between the molten metal and substrate, and they find that the pockets of entrapped air cause indentations on the bottom surface of molten metal. Liu et al. [10] also applied the numerical method to conduct thermal contact analysis for a molten metal drop impacting on a substrate, their results suggest that the type of substrate material effect the thermal contact coefficient a lot. The second way is to follow the method at the solid–solid contact conditions [5–8] to build theoretical models at the liquid–solid interface by conducting topographical and mechanical analyses at the interface [4,11–12]. Prasher [4] developed a surface chemistry model for the fluidic TIMs–solid contacts based on the definition of R_c proposed by Madhusudana [13]. The advantage of such model is taking into consideration the wettability of the liquid on rough surface and making mechanical analysis in detail. Thus the model successfully illustrated the interface characteristics at

* Corresponding author.
  E-mail address: Luoxb@hust.edu.cn (X. Luo).

Nomenclature

a_s	radius of microcontacts, m
b_s	radius of heat flux tube, m
BLT	bond line thickness, m
k	thermal conductivity, W m^{-1} K^{-1}
L	distance between the marks, m
m	slope of real surface profile
m_n	slope of modified surface profile
n_s	microcontacts density of solid surface, m^{-2}
P_b	applied pressure, Pa
P_γ	capillarity pressure of liquid, Pa
P_0	atmospheric pressure, Pa
q	heat flux, W m^{-2}
R_a	arithmetic average of the surface roughness, m
R_{bulk}	bulk thermal resistance of TIM, m^2 K W^{-1}
R_c	thermal contact resistance, m^2 K W^{-1}
R_q	root mean average of the surface roughness, m
R_{sm}	mean peak spacing, m
R_{tot}	total resistance at the TIM bond lines, m^2 K W^{-1}
r_c	thermal resistance of a single microcontact spot, K W^{-1}
r^2	correlation coefficients
T_0	atmospheric temperature, K
T_c	contact temperature at the liquid-solid interface, K

V_0, V_c	volume of the entrapped air before and after the liquid–solid contact, m^3
Y	height of the entrapped air after the liquid–solid contact, m
Greek	
σ	standard deviation of the asperities heights, m
$\phi(y)$	Gaussian distribution function of the heights of asperities
ε	factor related to the surface profile
γ	surface energy, N m^{-2}
θ	contact angle, deg
φ	angle between the cavity and mean plan, deg
ΔT	temperature difference of the bond lines, K
ΔR	error in measurement of thermal resistance, m^2 K W^{-1}
ΔBLT	error in measurement of BLT, m
Subscript	
1, 2	Sides
d	dispersion component of surface energy
l	Liquid
p	polar component of surface energy
s	Solid

---

the liquid–solid contact. The surface geometry assumption in this model is that the solid asperities are conical in shape with the same heights, and the spacing of the peaks and valleys is identical and equal to the roughness sampling interval [4]. However roughness sampling interval is a profilometer parameter that is used to modify the roughness measurement conditions [14]. On the other hand, Hamasaiid et al. [11–12] developed a predictive model for the casting-die interface based on the definition of R_c in CMY model [6]. The advantages of this model are assuming the asperity heights follow a Gaussian distribution which is more acceptable for exhibiting the surface geometry [6], and using mean asperity peak spacing (R_{sm}), measured by the profilometer, as the spacing of the peaks and valleys. Different from surface chemistry model, mechanical analysis in Hamasaiid et al. model are completed by evaluating the capillarity pressure of the molten alloy as a function of the applied pressure through experiments. Predictions of the model are found to agree with the experimental results.

According to the above review, Hamasaiid et al. model is found to have better topographical analysis, while wettability analysis in the surface chemistry model makes it characteristic-based and suitable for different types of liquid–solid interfaces. Thus the idea of this paper is to develop an improved model based on Hamasaiid et al. model by adopting the wettability analysis at the liquid–solid interface. This improved model is compared with the experimental results of R_c at the TIMs–solid interface.

2. Model of thermal contact resistance

2.1. Theoretical background

Fig. 1 schematically shows the formation of R_c at the fluidic TIM–solid interface. Heat flux passing from the solid to TIM or from TIM to solid needs to be constricted at the microcontact spots. At the macroscopic scale, it brings in a temperature difference at the interface resulting in a thermal resistance. Based on CMY model [6], the thermal field at the interface can be split into several identical isothermal flux tubes as illustrated in Fig. 1. The thermal resistance of a single microcontact spot can be determined from the following relationship [6]:

$$r_c = \frac{\left(1 - \frac{a_s}{b_s}\right)^{1.5}}{2k_s a_s} \tag{1}$$

where $k_s = 2k_1 k_2/(k_1 + k_2)$ is the effective thermal conductivity of the contacting bodies, a_s is the radius of the circular microcontact point and b_s is radius of the heat flux tube. Considering the microcontacts density n_s of the interface, the overall thermal resistance is the sum of all the single microcontact resistances which are connected in parallel:

$$R_c = \frac{r_c}{n_s} = \frac{\left(1 - \frac{\langle a_s \rangle}{\langle b_s \rangle}\right)^{1.5}}{2k_s n_s \langle a_s \rangle} \tag{2}$$

where $\langle a_s \rangle$ and $\langle b_s \rangle$ are the average radii of the microcontact points and the heat flux tubes, respectively. Eq. (2) has been widely accepted in the field of R_c. Following the ways of developing R_c model at the solid–solid contacts [5–8,15–19], $\langle a_s \rangle$, $\langle b_s \rangle$ and n_s can be estimated by topographical and mechanical analyses at
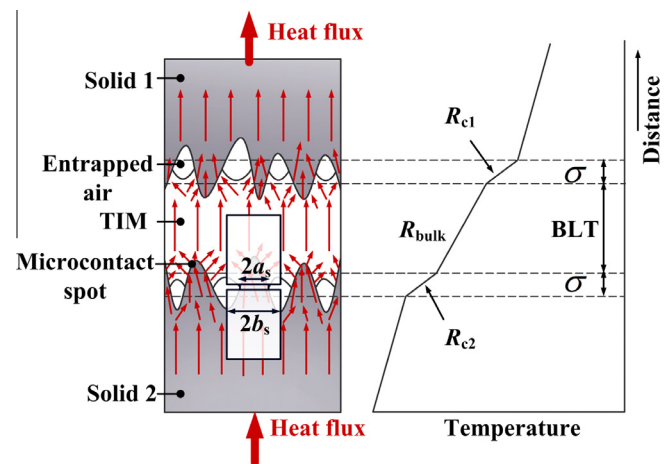

Fig. 1. Formation of R_c and the resistance components in the solid–TIM–solid structure.

liquid–solid contacts. In this paper, asperities resistance is neglected because it is small enough compared to R_c [12].

2.2. Topographical analysis

To describe the solid surface profile, three key surface roughness parameters are considered: the arithmetic mean deviation of the profile R_a, root-mean-square deviation of the profile R_q, and R_{sm}. Hamasaiid et al. [12] have made three assumptions to simplify the solid surface profile:

(1) The solid surface profile consists of successive peaks and valleys with the bases on the mean plane. The spacing of the peaks and valleys is identical and equal to R_{sm}.
(2) The asperities are conical in shape with the same slope (m).
(3) The heights of asperities (y) follow a Gaussian distribution with a distribution function $\phi(y)$ which is expressed as:

$$\phi(y) = \frac{1}{\sqrt{2\pi}\sigma} \exp\left(\frac{-y^2}{2\sigma^2}\right) \quad y \in (-\infty, +\infty) \tag{3}$$

Based on the standard definitions, R_a and R_q can be expressed as:

$$R_a = \int_{-\infty}^{+\infty} \phi(y)|y|dy \tag{4}$$

$$R_q = \sqrt{\int_{-\infty}^{+\infty} \phi(y)y^2 dy} = \sigma \tag{5}$$

Eq. (5) shows that R_q is equal to the standard deviation of the Gaussian distribution σ.

For the convenience of mechanical analysis, the model proposed by Hamasaiid et al. [12] modifies the real solid surface profile to a new profile as shown in Fig. 2. The modified surface profile has a common base for the asperities. Then all the valleys are brought to the same level ($y = 0$). The asperities are still conical in shape but with a new normalized slope (m_n). To keep initial surface roughness parameters (R_a, R_q, and R_{sm}) measured by profilometer constant, Hamasaiid et al. [12] propose a new height distribution of peaks $\phi_B(y)$ for the modified profile which is expressed by equation:

$$\phi_B(y) = \frac{2}{\sqrt{2\pi}\sigma} \exp\left(\frac{-y^2}{2\sigma^2}\right) \quad y \in [0, \infty+) \tag{6}$$

After the transformation of solid profile, the liquid–solid contact profile is shown in Fig. 3. The authors [12] have successfully developed the expressions of $\langle a_s \rangle$, $\langle b_s \rangle$ and n_s, respectively as follows:
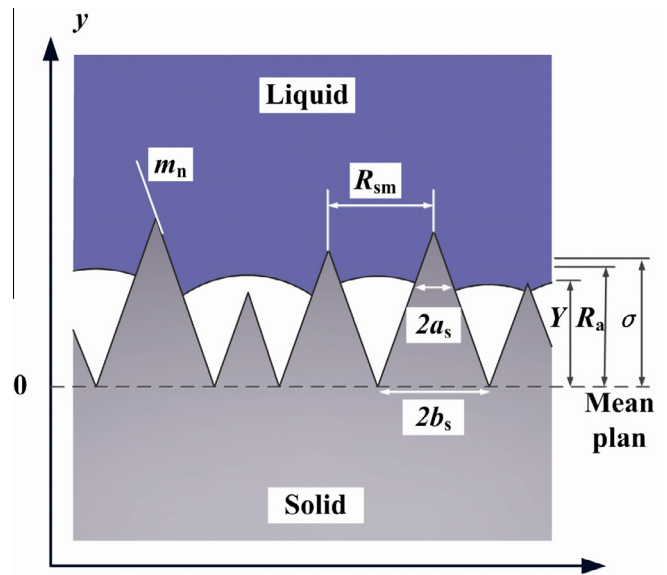

Fig. 3. Modified profile of the liquid–solid interface.

$$\langle a_s \rangle = \int_{y=Y}^{\infty} \frac{(y-Y)}{m_n} \phi_B(y)dy$$

$$= \frac{R_{sm}}{2}\left(\exp\left(-\frac{Y^2}{2\sigma^2}\right) - \sqrt{\frac{\pi}{2}}\frac{Y}{\sigma}\,\mathrm{erfc}\left(\frac{Y}{\sqrt{2}\sigma}\right)\right) \tag{7}$$

$$\langle b_s \rangle = \frac{R_{sm}}{2} \tag{8}$$

$$n_s = \frac{8}{\varepsilon\pi^2}\left(\frac{1}{R_{sm}}\right)^2 \mathrm{erfc}\left(\frac{Y}{\sqrt{2}\sigma}\right) \tag{9}$$

where Y is the mean height of the entrapped air, ε is a factor determined statistically to be close to 1.5 [12] and m_n is given by:

$$m_n = 2\sqrt{\frac{2}{\pi}}\frac{\sigma}{R_{sm}} \tag{10}$$

By substituting Eqs. (7)–(9) to Eq. (2), the thermal contact resistance is determined as follow:

$$R_c = \frac{\left(1 - \left(\exp\left(-\frac{Y^2}{2\sigma^2}\right) - \sqrt{\frac{\pi}{2}}\frac{Y}{\sigma}\mathrm{erfc}\left(\frac{Y}{\sqrt{2}\sigma}\right)\right)\right)^{1.5}}{\frac{8k_s}{1.5\pi^2 R_{sm}}\mathrm{erfc}\left(\frac{Y}{\sqrt{2}\sigma}\right)\left(\exp\left(-\frac{Y^2}{2\sigma^2}\right) - \sqrt{\frac{\pi}{2}}\frac{Y}{\sigma}\mathrm{erfc}\left(\frac{Y}{\sqrt{2}\sigma}\right)\right)} \tag{11}$$
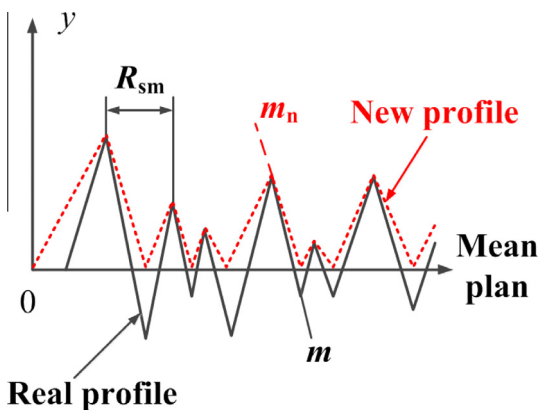

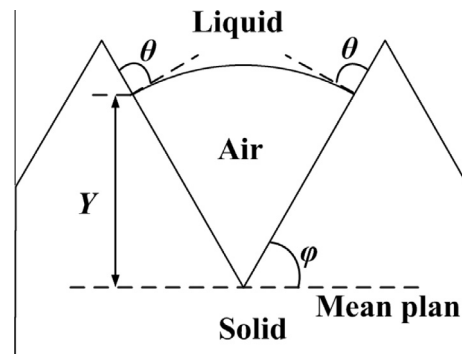**Fig. 2.** Real and new surface profiles.

Fig. 4. Spreading of a liquid material on the solid rough surface.

According to the above equations, R_c is a function of k_s, surface roughness (σ, R_{sm}) and Y. To determine Y, mechanical analysis should be done at the contacting interface.

2.3. Mechanical analysis

Fig. 4 shows the wetting of the liquid on the solid rough surface. When liquid material impinges on the solid surface, it spreads out and wets the microcavity inside which the air is then compressed. An equilibrium state is established at the liquid–solid interface between the applied pressure P_b, the capillarity pressure P_γ due to the liquid surface energy, and the back pressure of air P_0. Assuming the entrapped air is ideal gas and not allowed to escape, the ideal gas equation can express the equilibrium as follow:

$$\frac{(P_b \pm P_\gamma)V_c}{T_c} = \frac{P_0 V_0}{T_0} \tag{12}$$

where V_0 and V_c are the volume of the entrapped air before and after the liquid–solid contact, T_0 and T_c are the initial and contact temperature at the interface, + or − means good or poor surface wetting, respectively. To solve Eq. (12), P_γ must be given first. In Hamasaiid et al. model [12], an empirical expression of P_γ has been evaluated through experiments at the casting–die interface. In this paper, we try to adopt the wettability analysis of surface chemistry model to solve this problem. In surface chemistry model [4], P_γ is found to be determined by the surface tension of liquid, wetting conditions, and the topography of microcavity. For this problem, P_γ is given by [4]:

$$P_\gamma = \frac{2\gamma_l \sin(\theta + \varphi)}{Y \cot(\varphi)} \tag{13}$$

where γ_l is the surface energy of liquid, θ is the contact angle of liquid on solid surface and φ is the angle between the cavity and mean plan which can be expressed as:

$$\varphi = \arctan(m_n) \tag{14}$$

According to the above topographical analysis and assumption that the entrapped air is conical in shape, the average values of V_0 and V_c can be expresses as [12]:

$$V_c = \frac{1}{3}\pi \frac{1}{m_n^2} \int_{y=0}^{Y} \phi_B(y) y^3 dy \approx \frac{\pi Y^3}{3 m_n^2} \tag{15}$$

$$V_0 = \frac{1}{3}\pi \frac{1}{m_n^2} \int_{y=0}^{\infty} \phi_B(y) y^3 dy = \frac{2\pi}{3}\sqrt{\frac{2}{\pi}}\frac{\sigma^3}{m_n^2} \tag{16}$$

By substituting Eqs. (13), (15 and 16) to Eq. (12), the equilibrium equation can be expressed as follows:

$$\left(P_b \pm \frac{2\gamma_l \sin(\theta + \varphi)}{Y \cot(\varphi)}\right)\frac{1}{T_c} = \frac{P_0}{T_0}\frac{V_0}{V_c} = \frac{P_0}{T_0}\frac{2\sqrt{\frac{2}{\pi}}\sigma^3}{Y^3} \tag{17}$$

For the contact angle of fluidic TIMs on substrate is less than 90°, which will be illustrated in detail in Section 3.3, this paper deals with the good wetting condition. Thus Eq. (17) can be solved to determine the Y for the microcavities:

$$Y \approx \frac{1}{\Gamma + \frac{2\gamma_l \sin(\theta+\varphi)}{3\Gamma P_0 Y_0^3 \chi \cot(\varphi)}} \tag{18}$$

where

$$\Gamma = \left(\left(\frac{P_b^2}{4P_0^2 Y_0^6 \chi^2} - \frac{8\gamma_l^3 \sin^3(\theta + \varphi)}{27 P_0^3 Y_0^9 \chi^3 \cot^3(\varphi)}\right)^{1/2} + \frac{P_b}{2P_0 Y_0^3 \chi}\right)^{1/3} \tag{19}$$

$$\chi = \frac{T_c}{T_0} \tag{20}$$

Eqs. (18)–(20) shows that Y depends on applied pressure (P_b), wetting ability (γ_l, θ), topography of the solid surface (σ, m_n) and temperature (T_c, T_0). These parameters together with R_{sm} and k_s determine the R_c according to Eq. (11). In the following, we will validate the improved model via experiments and discuss the influences of σ, R_{sm}, k_s and P_b on R_c in detail.

3. Experiment for the measurement of R_c

3.1. Experimental principles

Experimental measurements are conducted on three layers structure as shown in Fig. 1. The total resistance R_{tot} at the TIM bond lines can be expressed as:

$$R_{tot} = \frac{\Delta T}{q} = R_{bulk} + R_{c1} + R_{c2} \tag{21}$$

where ΔT is the temperature difference of the bond lines, q is the heat flux through the bond lines, R_{bulk} is equal to the ratio of bond line thickness (BLT) to thermal conductivity of TIM (k_{TIM}), and R_{c1} is equal to R_{c2} when the roughness of upper and lower substrates are assumed to be identical. Thus, R_{tot} can be given by:

$$R_{tot} = \frac{1}{k_{TIM}}BLT + 2R_c \tag{22}$$

From Eq. (22), Fig. 5 shows the plots of R_{tot} versus BLT for multiple materials. It can be seen that collecting R_{tot} data over a range of BLT will create a linear relation with a slope $1/k_{TIM}$ and a vertical axis intercept $2R_c$. Thus, based on this principle, both k_{TIM} and R_c can be measured.

3.2. Thermal and BLT measurement

The R_c and k_{TIM} were measured using a thermal interface material testing system which is based on ASTM D 5470 standard [20]. Fig. 6 illustrates the sketch of testing system consisting of five main components: heat flux meters, heating and cooling units, load fixture, insulation materials, and the camera to measure the BLT.
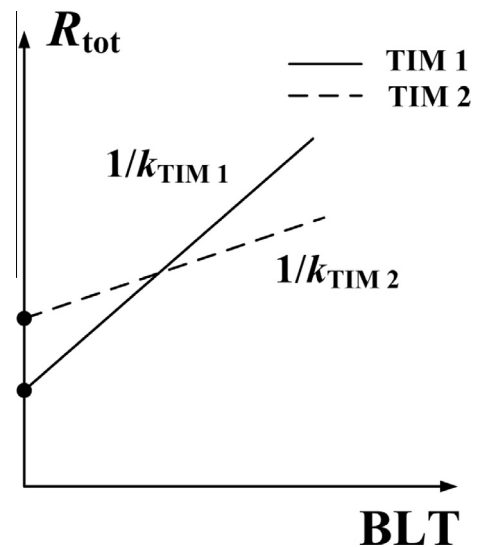

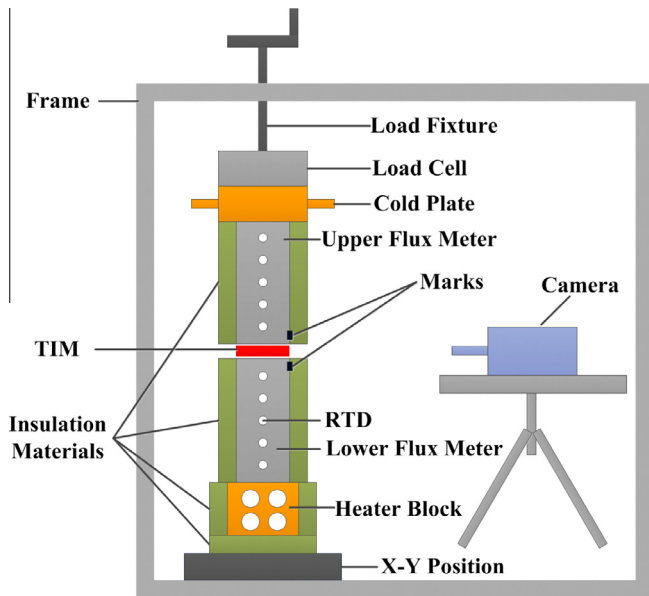**Fig. 5.** Plots of R_{tot} versus BLT for multiple materials.

Fig. 6. Sketch of the testing system.

Fig. 7. Use of shims to control BLT.

Heat flow through the specimen is measured by the heat flux meters with a 30 mm × 30 mm cross sectional area. It is accomplished by measuring the linear temperature gradient dT/dx in the heat flux meters and using the Fourier's law of heat conduction $q = k(dT/dx)$. The centerline temperature is measured at 10 mm intervals along each of the flux meter using five 1.5 mm diameter platinum resistance temperature detectors (RTDs).

Power is applied by a heater block embedded with four wire wound cartridge heaters capable of 120 W. A water-cooled heat sink is designed to remove the heat rejected from the upper heat flux meter. The design uses a micro-pump with a maximum flow rate 2.3×10^{-5} m^3/s to circulate water. Consequently heat flow in flux meter is assured to be one-dimensional. The contact pressure on the specimen is controlled by the lead screws. A load cell with a resolution 3.3 kPa continuously monitors the applied load.

Insulation tapes with a thermal conductivity of 0.034 W m^{-1} K^{-1} and a thickness of 6 mm is placed around four sides of the heat flux meters to ensure the heat flow through the lower and upper meters varies by less than 5%. 10 mm thick firebond insulation is placed around four sides of heat block to eliminate heat leakage to the environment. Heat loss from the bottom is minimized by attaching it to 10 mm thick FR-4 epoxy material.

A camera with a microscope lens is implemented to measure BLT, as well as to detect the parallelism of the interface before the start of each test. Two 1 mm × 1 mm square marks are attached to the upper and lower flux meters located approximately 2 mm from the flux meters edges. These marks are used as targets and the camera measures the distance between the centers of the targets. These marks are scanned in an approximately 5 mm field of view. The camera provides 1024 × 1024 bit resolution and each pixel is approximately 5 μm in length, so the resolution of BLT measurement is limited to 5 μm. There are two steps to measure BLT. The first step is to apply a 1 MPa load between the heat flux meters without TIM and measure the targets distance L_0. The second step is to separate the flux meters, fill the TIM between the flux meters and measure the targets distance L_1 at the desired pressure. Then BLT is calculated by subtracting the L_0 from L_1.

For the measurement of R_c and k_{TIM}, BLT of TIMs needs to be controlled so that R_{tot} can be measured for a range of BLT as mentioned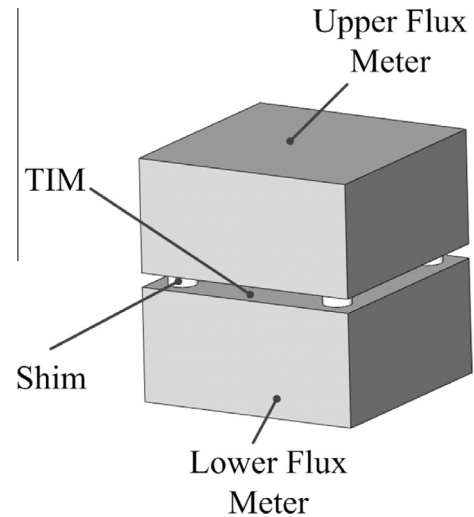 above. In this experiment, stainless steel shims are mixed into the TIMs to control the thickness as shown in Fig. 7. The shims are 1.5 mm in diameter, and the thermal conduction through them is negligible which has been verified by Prasher et al. [21]. Although the pressure from lead screws is applied on the sample, the shims take most of the pressure.

3.3. Sample preparation

Aluminium-6061 T4 blocks were chosen as the solid substrates, as well as the heat flux meters. The thermal conductivity is 154 W m^{-1} K^{-1}. Four couples of blocks were machined with different surface roughness. For each couple, surface roughness parameters are measured by a Mitutoyo SJ-401 surface profilometer for 12 times, and we set the average value as the roughness of the couple. Shin Etsu KF96H silicone oil and Dow Corning TC5121 thermally conductive grease are prepared for the TIMs. Because this experiment can measure the thermal conductivity, the average values of experimental results are set to be their thermal conductivities. Eight experimental combinations of substrates roughness and TIMs are shown in Table 1.

The surface energy of the silicone oil was provided by the supplier, and that of the grease and aluminium substrate is measured with standard two liquid method using water and diiodomethane (CH$_2$I$_2$) based on the ASTM D 7490 standard [22]. This method can measure the polar and dispersion components of the material surface energy, γ_p and γ_d, respectively. The total surface energy of the material is the sum of γ_p and γ_d. The contact angle of silicone oil was directly measured on the smoothest aluminium substrate by sessile drop method [23]. However, because thermal grease has extremely high viscosity, the method cannot be used for grease. The contact angle of grease on the aluminium substrate can be calculated by using the equation [23]:

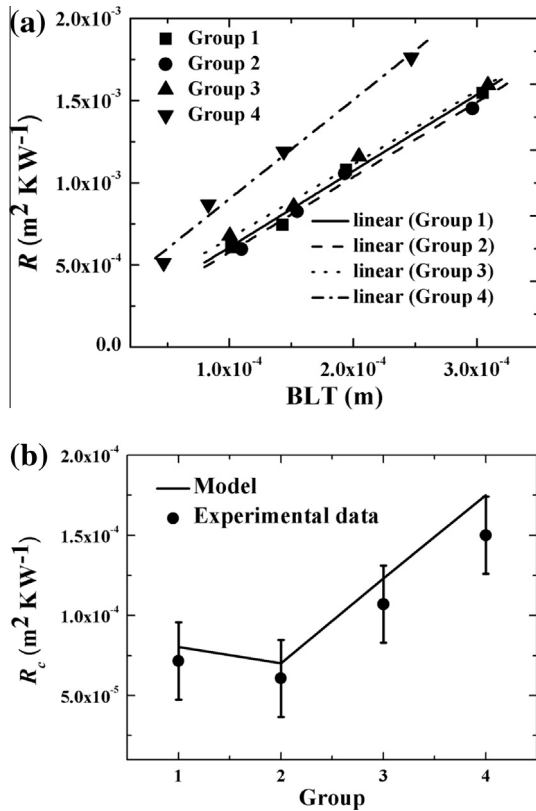$$(1 + \cos\theta)\gamma_l = 2\sqrt{\gamma_{lp}\gamma_{sp} + \gamma_{ld}\gamma_{sd}} \tag{23}$$

where the subscripts l and s refer to the liquid and substrate, respectively. Because γ_p and γ_d of the grease and substrate have been measured, the contact angle can be calculated. Table 2 shows the surface energy of silicone oil, thermal grease, and aluminium block, and the contact angle of silicone oil and thermal grease on the aluminium block.

Table 1
Experimental combinations for the measurement of R_c.

Materials		Silicone oil ($k_{TIM\ 1}$)	Grease ($k_{TIM\ 2}$)
Aluminium 154 W m^{-1} K^{-1}	σ = 0.23 μm R_{sm} = 99.2 μm	1	5
	σ = 0.34 μm R_{sm} = 90.8 μm	2	6
	σ = 0.72 μm R_{sm} = 132.1 μm	3	7
	σ = 1.13 μm R_{sm} = 166.4 μm	4	8

Table 2
Surface energy of TIMs and aluminium block, and the contact angle of TIMs on the block.

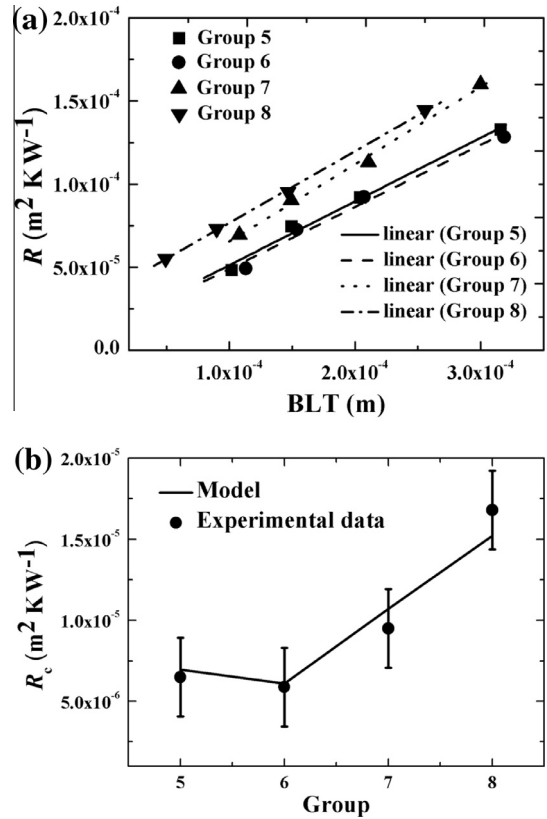|	Silicone oil	Thermal grease	Aluminium block
γ_p (mN m^{-1})	–	24.2	41.6
γ_d (mN m^{-1})	–	14.0	4.2
γ (mN m^{-1})	21.3	38.2	45.8
θ (deg)	22.3	45.0	–

Fig. 8. (a) Plots of thermal resistance R versus BLT; (b) Comparison of the model results with experimental data for silicone oil.

Fig. 9. (a) Plots of thermal resistance R versus BLT; (b) Comparison of the model results with experimental data for thermal grease.

Table 3
Linear regression equations and correlation coefficients of all groups.

Group	Linear regression equations	Correlation coefficients r^2
1	$R = 4.64 \times BLT + 1.431 \times 10^{-4}$	0.9970
2	$R = 4.57 \times BLT + 1.217 \times 10^{-4}$	0.9899
3	$R = 4.49 \times BLT + 2.140 \times 10^{-4}$	0.9949
4	$R = 6.02 \times BLT + 3.003 \times 10^{-4}$	0.9872
5	$R = 0.383 \times BLT + 1.299 \times 10^{-5}$	0.9911
6	$R = 0.373 \times BLT + 1.175 \times 10^{-5}$	0.9856
7	$R = 0.465 \times BLT + 1.898 \times 10^{-5}$	0.9952
8	$R = 0.431 \times BLT + 3.369 \times 10^{-5}$	0.9991

3.4. Error analysis

According to Eq. (22), the error in R_c is given as [24]

$$\frac{\Delta R_c}{R_c} = \pm \sqrt{\left(\frac{\Delta R}{(R_{tot} - BLT/k_{TIM})/2}\right)^2 + \frac{1}{k_{TIM}^2}\left(\frac{\Delta BLT}{(R_{tot} - BLT/k_{TIM})/2}\right)^2}$$

(24)

Following the method in Ref. [25], the errors in R for the silicone oil and grease are measured with 3.8×10^{-6} m^2 K W^{-1} and 1.3×10^{-6} m^2 K W^{-1}, respectively. The error in BLT is 5 μm which is equal to the pixel size of the camera.

4. Validation and discussion

4.1. Comparison of experimental data with the model

For the all experimental combinations, experiments were conducted for four different BLTs to find out R_c and k_{TIM}. Figs. 8 and 9(a) show the plots of thermal resistance R versus BLT for the silicone oil and thermal grease, respectively. It is shown that R is linearly dependent on BLT, thus R_c and k_{TIM} can be computed by the linear least square method. The solved linear regression equations and correlation coefficients are given in Table 3. According to
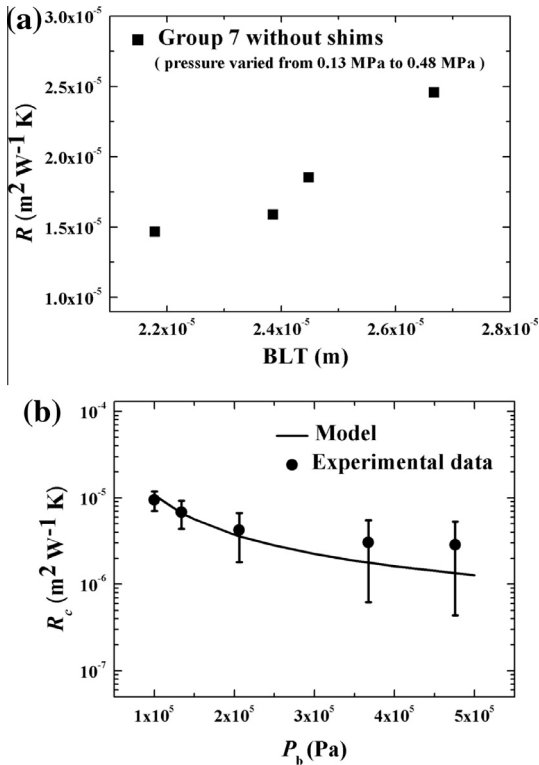
Fig. 10. (a) Scatters of thermal resistance R versus BLT for the group 7 with difference applied pressures; (b) Comparison of the model results with experimental data.

Eq. (22), thermal conductivity of silicone oil can be obtained by taking the average of the 1/slope of the groups 1 to 4 linear equations, which is equal to 0.21 W m^{-1} K^{-1}. In the same way, thermal conductivity of grease can be computed, which is equal to 2.44 W m^{-1} K^{-1}. Meanwhile, R_c for each group can be obtained by taking half of the intercept of the linear regression equations. Figs. 8 and 9(b) show the experimental results of R_c for the silicone oil and thermal grease, respectively, as well as the error bars. According to Eq. (24), the biases of silicone oil and grease from the experiments are 2.41×10^{-5} m^2 K W^{-1} and 2.43×10^{-6} m^2 K W^{-1}, respectively.

As mentioned above, predicting R_c needs to obtain the parameters as follow: topography parameters (σ, R_{sm}), wettability parameters (γ_l, θ), mechanical parameter (P_b), and thermal parameters
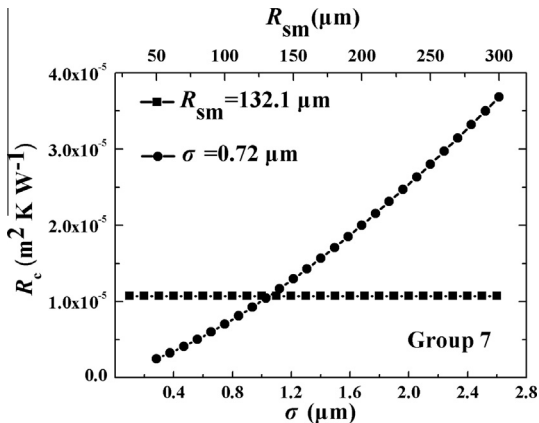

Fig. 11. Variation of R_c with σ and R_{sm} respectively when one of them keeps constant.
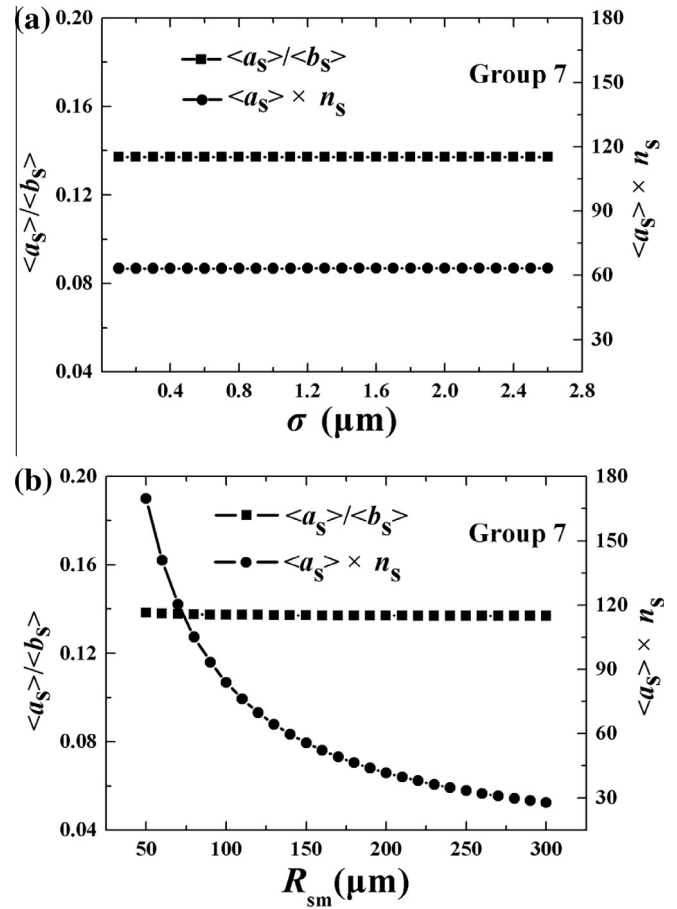

Fig. 12. Variation of $\langle a_s \rangle / \langle b_s \rangle$ and $\langle a_s \rangle \times n_s$ with (a) σ when R_{sm} keeps constant; (b) R_{sm} when σ keeps constant.

(k_s, T_0, T_c). In the experiments of groups 1 to 8, P_b is 0.1 MPa, T_0 is 288 K, and T_c is approximately 323 K by taking the average temperature of the TIMs in the testing. Other parameters can be obtained in Tables 1 and 2. Figs. 8 and 9(b) show the model results of R_c for all groups. Compared with the experimental results, it can be found that the improved model matches well with experimental data. The deviation between the experimental and model results is less than 14.3%.

In order to study the influence of P_b on R_c, different pressures varied from 0.13 MPa to 0.48 MPa were set on group 7 without the shims controlling the BLT. Fig. 10(a) shows the scatters of
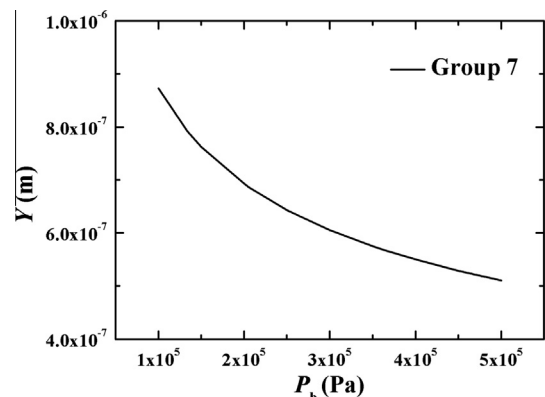

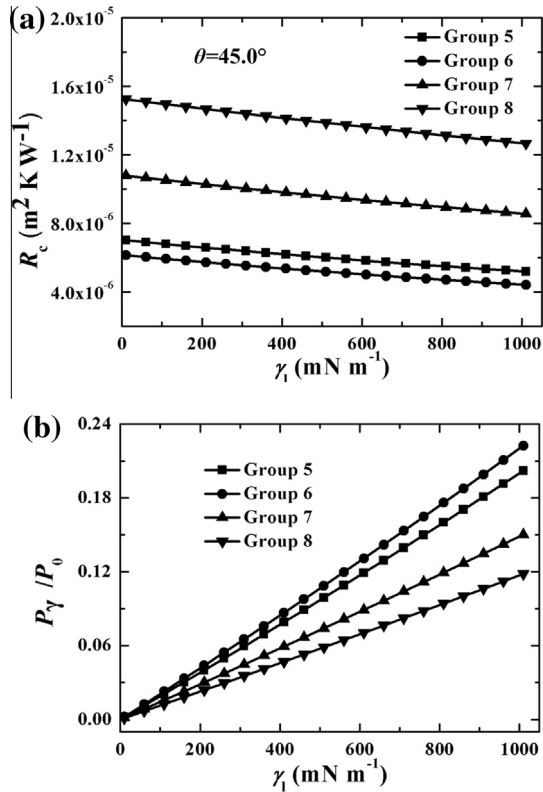**Fig. 13.** Variation of Y as a function P_b.

Fig. 14. (a) Variation of R_c and (b) P_γ/P_0 with γ_l when θ keeps constant.
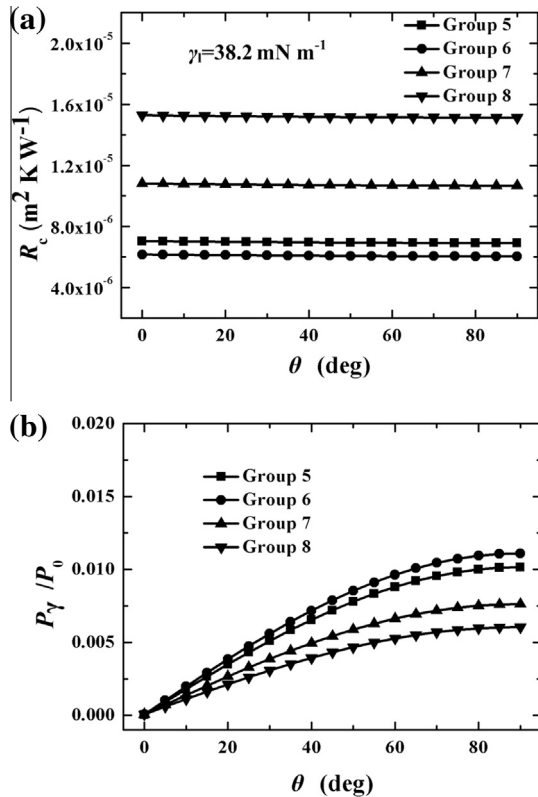

Fig. 15. (a) Variation of R_c and (b) P_γ/P_0 with θ when γ_l keeps constant.

measured R versus measured BLTs. Based on Eq. (22), the values of R_c with various pressures can be computed. Fig. 10(b) shows the comparison between the experimental and model results. At lower pressure, the model matches well with experimental results. But the model predictions tend to deviate at higher pressure owing to the higher relative error in thin BLT measurement.

4.2. Influence of the parameters on the model results

In the Ref. [12], the authors have highlighted the effect of surface roughness on R_c in liquid–solid interface. According to their predictive model, σ does not have any influence on R_c, while R_{sm} has more effect on R_c. Similar results can be found in the improved model. Using the parameters of group 7, Fig. 11 respectively presents the curves of R_c versus σ and R_{sm} when one of them keeps constant. It is shown that R_c changes hardly with σ, but increases with R_{sm} obviously. In order to explain the results, Fig. 12 shows the plots of $\langle a_s \rangle / \langle b_s \rangle$ and $\langle a_s \rangle \times n_s$ as a functions of σ and those as a functions of R_{sm}. When R_{sm} keeps constant, σ nearly has no significant influence on $\langle a_s \rangle / \langle b_s \rangle$ or $\langle a_s \rangle \times n_s$. Thus R_c does not change with σ according to Eq. (2). Contrary to σ, the larger the value of R_{sm}, the smaller the $\langle a_s \rangle \times n_s$. And the $\langle a_s \rangle / \langle b_s \rangle$ still remains constant so that R_c turns larger according to Eq. (2). Comparing the R_c between groups 1 and 2 in Fig. 8(b), or between groups 5 and 6 in Fig. 9(b), the experimental results seem to be accorded with the claim that R_{sm} has the more important impact on R_c. However, the considerable experimental bias and the limited experimental samples fail to make it credible enough to verify the point. Thus it is desired to investigate this work in the future to validate the results of the improved R_c model.

Comparing the predictive results of R_c between the groups having the same roughness parameters, such as groups 1 and 5, groups 2 and 6, and so on, it can be found that R_c is approximately inversely proportional to thermal conductivity of TIMs. Thermal conductivity of aluminium is much larger than k_{TIM} and this makes k_s approximately equal to $2k_{TIM}$. Then Eq. (2) shows R_c varies in an inverse proportion to k_{TIM}.

As illustrated in Fig. 10(b), R_c decreases with P_b increasing. To better understand the effect of P_b on R_c, Y is plotted as a function of P_b and it is shown in Fig. 13. It shows that Y decreases with P_b increasing. Thus higher P_b makes the liquid and solid contact better and result in a lower R_c at the interface.

Finally, the effect of wettability parameters (γ_l, θ) on R_c is investigated. Figs. 14 and 15(a) respectively presents the curves of R_c versus γ_l and θ for the groups 5–8. From Fig. 14(a), it is seen that R_c tendentially decreases with γ_l increasing when θ is equal to 45.0°. Fig. 14(b) plots P_γ/P_0 as a function of γ_l. The figure shows that P_γ increases with γ_l increasing. Then Y decreases according to Eq. (18) and finally R_c decreases. From the figure, it can be also found that the larger R_{sm} is, the lower P_γ is. On the other hand, Fig. 15(a) shows a very slow decrease of R_c with θ increasing when γ_l is relatively small and equal to 38.2 mN m^{-1}. In order to explain the results, P_γ/P_0 is plotted as a function of θ as shown in Fig. 15(b). It shows that P_γ increase with θ increasing. However the value of P_γ is much smaller than P_0 which means P_γ makes less contribution to Y. So for the materials with small γ_l, R_c hardly changes with θ.

5. Conclusion

This paper proposes an improved model for predicting thermal contact resistance R_c at the liquid–solid interface based on Hamasaiid et al. model. Through conducting the wettability analysis on the liquid–solid contact, an explicit expression is derived to predict the height of entrapped air between the liquid and solid. Experimental measurements have been conducted on TIMs-aluminium

interface. The results show the model matches well with the experimental data.

The proposed model shows that compared to standard deviation of the asperities heights σ, the mean asperity peak spacing R_{sm} has more effect on R_c, and R_c decreases with R_{sm}. It is observed that R_c varies with thermal conductivity of TIMs k_{TIM} in an inverse proportion, when the thermal conductivity of solid substrate is much larger than k_{TIM}. The extrapolation of the height of the entrapped air Y has shown that it is directly dependent on applied pressure P_b. Higher P_b can make liquid and solid contact better and results in a lower R_c. R_c tendentially decreases with surface energy of liquid γ_l. For the materials with small γ_l, R_c hardly changes with contact angle of liquid on solid surface θ.

Conflict of interest

None declared.

Acknowledgements

References

[1] R.S. Prasher, J. Shipley, S. Prstic, P. Koning, J.L. Wang, Thermal resistance of particle laden polymeric thermal interface materials, J. Heat Transfer 125 (6) (2003) 1170–1177.

[2] R.S. Prasher, Rheology based modeling and design of particle laden polymeric thermal interface materials, IEEE Trans. Compon. Packag. T. 28 (2) (2005) 230–237.

[3] R.S. Prasher, Thermal interface materials: historical perspective, status, and future directions, Proc. IEEE 94 (8) (2006) 1571–1586.

[4] R.S. Prasher, Surface chemistry and characteristic based model for the thermal contact resistance of fluidic interstitial thermal interface materials, J. Heat Transfer 123 (5) (2001) 969–975.

[5] C.R. Tien, A correlation for thermal contact conductance of nominally-flat surfaces in vacuum, in: Proc. 7th Thermal Conductivity Conference, U. S. Bureau of Standards, 1968, pp. 755–759.

[6] M.G. Cooper, B.B. Mikic, M.M. Yovanovich, Thermal contact conductance, Int. J. Heat Mass Transfer 12 (3) (1969) 279–300.

[7] T.R. Thomas, S.D. Probert, Thermal contact resistance: the directional effect and other problems, Int. J. Heat Mass Transfer 13 (5) (1970) 789–807.

[8] B.B. Mikic, Thermal contact conductance: theoretical considerations, Int. J. Heat Mass Transfer 17 (2) (1974) 205–214.

[9] T. Bennett, P. Poulikakos, Heat transfer aspects of splat-quench solidification: modelling and experiment, J. Mater. Sci. 29 (8) (1994) 2025–2039.

[10] W. Liu, G.X. Wang, E.F. Matthys, Thermal analysis and measurements for a molten metal drop impacting on a substrate: cooling, solidification and heat transfer coefficient, Int. J. Heat Mass Transfer 38 (8) (1995) 1387–1395.

[11] A. Hamasaiid, G. Dour, T. Loulou, M. Dargusch, A predictive model for the evolution of the thermal conductance at the casting-die interfaces in high pressure die casting, Int. J. Therm. Sci. 49 (2) (2010) 365–372.

[12] A. Hamasaiid, M. Dargusch, T. Loulou, G. Dour, A predictive model for the thermal contact resistance at liquid–solid interfaces: analytical developments and validation, Int. J. Therm. Sci. 50 (8) (2011) 1445–1459.

[13] C.V. Madhusudana, Thermal Contact Conductance, Springer-Verlag, New York, 1996.

[14] SJ-401 Surface Roughness Tester User's Manual, Mitutoyo Corporation, Japan.

[15] M.R. Sridhar, M.M. Yovanovich, Review of elastic and plastic contact conductance models: comparison with experiment, J. Thermophys. Heat Transfer 8 (4) (1994) 633–640.

[16] M.R. Sridhar, M.M. Yovanovich, Elastoplastic contact conductance model for isotropic conforming rough surfaces and comparison with experiments, J. Thermophys. Heat Transfer 118 (1) (1996) 3–9.

[17] M. Bahrami, M.M. Yovanovich, J.R. Culham, Thermal joint resistances of nonconforming rough surfaces with gas-filled gaps, J. Thermophys. Heat Transfer 18 (3) (2004) 326–332.

[18] M. Bahrami, J.R. Culham, M.M. Yovanovich, G.E. Schneider, Thermal contact resistance of nonconforming rough surfaces, part 1: contact mechanics model, J. Thermophys. Heat Transfer 18 (2) (2004) 209–217.

[19] M. Bahrami, J.R. Culham, M.M. Yovanovich, G.E. Schneider, Thermal contact resistance of nonconforming rough surfaces, part 2: thermal model, J. Thermophys. Heat Transfer 18 (2) (2004) 218–227.

[20] ASTM Standard D-5470-06, Standard test method for thermal transmission properties of thermally conductive electrical insulation materials, Copyright ASTM International, Conshohocken, PA, 2007.

[21] R.S. Prasher, P. Koning, J. Shipley, A. Devpura, Dependence of thermal conductivity and mechanical rigidity of particle-laden polymeric thermal interface material on particle volume fraction, J. Electron. Packag. 125 (3) (2003) 386–391.

[22] ASTM Standard D-7490-13, Standard test method for measurement of the surface tension of solid coatings, substrates and pigments using contact angle measurements, Copyright ASTM International, Conshohocken, PA, 2013.

[23] S. Wu, Polymer Interface and Adhesion, Marcel Dekker, New York, 1982.

[24] S.J. Kline, F.A. McClintock, Describing uncertainties in single sample experiments, Mech. Eng. 75 (1953) 3–8.

[25] R.S. Prasher, C. Simmons, G. Solbrekken, Thermal contact resistance of phase change and grease type polymeric materials, in: Proceedings of International Mechanical Engineering Congress and Exposition, Orlando, Florida, 2000.